ACS Catalysis

Research Article

pubs.acs.org/acscatalysis

# Experimental and Computational Investigation of Effect of Sr on NO Oxidation and Oxygen Exchange for $La_{1-x}Sr_xCoO_3$ Perovskite Catalysts

Sang Ok Choi,[†] Michael Penninger,[‡] Chang Hwan Kim,*[,§] William F. Schneider,*[,‡,∥] and Levi T. Thompson*[,†]

[†]Department of Chemical Engineering and Hydrogen Energy Technology Laboratory, University of Michigan, Ann Arbor, Michigan 48109-2136, United States

[‡]Department of Chemical and Biomolecular Engineering and [∥]Department of Chemistry and Biochemistry, University of Notre Dame, Notre Dame, Indiana 46556, United States

[§]General Motors Global R&D, Warren, Michigan 48090, United States

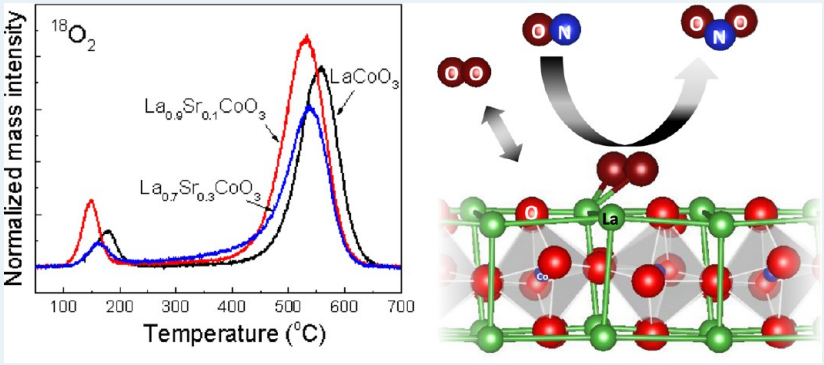


**ABSTRACT:** NO oxidation rates over $La_{1-x}Sr_xCoO_3$ ($x = 0-0.3$) perovskite catalysts are reported as a function of Sr doping in the absence and presence of $NO_2$ in the feed. Sr substitution is found to increase the rate of oxidation and to diminish the inhibitory influence of $NO_2$. Temperature programmed desorption and isotopic exchange (TPIE) experiments were used to identify surface species and oxygen exchange processes expected to correlate with NO oxidation activity. Oxygen exchange in the $LaCoO_3$ perovskites occurred primarily through a heteroexchange process that was enhanced by doping with Sr. Density functional theory (DFT) calculations were used to further investigate the oxygen exchange processes on (100) facets of undoped and doped $LaCoO_3$. Vacancy formation is predicted to be more facile on $CoO_2$-terminated than LaO-terminated surfaces. The Sr dopant segregates to the LaO-terminated surface and diminishes oxygen bonding consistent with the TPIE results. The results suggest a model in which multiple oxygen species contribute to low- and high-temperature oxygen exchange.

**KEYWORDS:** *NO oxidation, perovskites, Sr substitution, oxygen mobility, isotope exchange, $NO_2$ inhibition*

## 1. INTRODUCTION

Systems where combustion is carried out in excess air (lean) offer significant fuel efficiency benefits over systems operating under fuel rich conditions. Operation under lean conditions can contribute to a reduction in greenhouse gas emissions.[1] $NO_x$ ($x = 1, 2$) is an unavoidable byproduct of lean combustion. While cost-effective technologies have been demonstrated for the remediation of $NO_x$ produced at stationary sources including coal-fired power plants, the aftertreatment of $NO_x$ produced by mobile sources including diesel powered vehicles remains a major challenge. By some accounts, the lack of cost-effective NO aftertreatment systems and technologies is the key obstacle to broader implementation of diesel engines.[2]

The catalytic oxidation of NO to $NO_2$

$$NO(g) + \frac{1}{2}O_2(g) \leftrightarrow NO_2(g) \quad \Delta H^\circ = -57.2\ \text{kJ/mol} \tag{1}$$

is a key step in virtually all lean-burn $NO_x$ aftertreatment technologies,[3] including lean $NO_x$ traps (LNT)[4] and selective catalytic $NO_x$ reduction (SCR).[5] Platinum-based catalysts have been widely used for NO oxidation[6] and are, in fact, the only commercially available catalysts for mobile applications. Recently, Sr-promoted La-based perovskite catalysts ($La_{1-x}Sr_xCoO_3$) have been reported to possess NO oxidation activities that are superior to those for commercial Pt-based catalysts.[3] These observations are particularly noteworthy

Received: July 11, 2013
Revised: August 30, 2013
Published: September 16, 2013

  

because perovskite- and other oxide-based catalysts are much less expensive than Pt Group Metal based catalysts and have typically been found to be much less active for NO oxidation than Pt-based catalysts at moderate temperatures (near 300 °C).[7]

The catalytic oxidation activity is intimately connected to molecular and atomic interactions of oxygen with the oxide surface.[8] Catalytic oxidations over metal oxides are often rationalized in terms of a Mars−van Krevelen mechanism[9] in which vacancies in the oxide lattice facilitate the adsorption and dissociation of $O_2$:

$$2{-}M{-}\square{-}M{-}+O_2 \rightarrow 2{-}M{-}O{-}M{-} \quad (2)$$

Subsequent reaction with a reductant (R) reforms the vacancies to complete the catalytic cycle:

$$R + {-}M{-}O{-}M{-} \rightarrow R{-}O + {-}M{-}\square{-}M{-} \quad (3)$$

Given the Mars−van Krevelen mechanism, enhancements in the oxidation activities of oxide-based catalysts have often been attributed to enhanced oxygen vacancy densities.[10] Seiyama et al. and Tanaka et al. argued that the increased reducibility and oxidation activity of $La_{1-x}Sr_xCoO_3$ as compared to $LaCoO_3$ can be attributed to the density of oxygen desorbed from or absorbed to oxygen vacancies.[11] Other oxides, including rutile $RuO_2$, are known to activate oxygen through an extra-lattice mechanism with the reaction proceeding via Langmuir−Hinshelwood kinetics.[12] This extra-lattice oxygen based mechanism has been implicated in simulations of NO oxidation over Pd oxide;[13] experimentally observed kinetics have been interpreted in terms of a mechanism involving sparse vacancies on oxide surfaces nearly saturated with adsorbed oxygen.[14]

Isotopic oxygen exchange experiments can provide insights into the energetics and mechanisms associated with oxygen activation and reactivity on catalytic surfaces. Boreskov[15] and Winter[16] distinguished three types of isotopic oxygen exchange with oxides. Homoexchange involves exchange of oxygen in the gas phase without participation of oxygen from the surface:

$$^{18}O_2(g) + {}^{16}O_2(g) \leftrightarrow 2\,{}^{18}O{}^{16}O(g) \quad (4)$$

Simple heteroexchange involves exchange of an oxygen atom on the solid surface with oxygen from $O_2$

$$^{18}O_2(g) + {}^{16}O(s) \leftrightarrow {}^{18}O{}^{16}O(g) + {}^{18}O(s) \quad (5)$$

Finally there is multiple heteroexchange where oxygen is exchanged between a gaseous $O_2$ molecule and two oxygen atoms in the solid

$$^{18}O_2(g) + 2\,{}^{16}O(s) \rightarrow {}^{16}O_2(g) + 2\,{}^{18}O(s) \quad (6)$$

The oxygen exchange rate could provide insights regarding the role that Sr plays in enhancing the NO oxidation activities of $La_{1-x}Sr_xCoO_3$ perovskites.

First principles molecular models have been used extensively to understand catalytic oxidations on metal oxides. Most of the computational work on the perovskite oxides has used density functional theory (DFT) and has focused on the structure, energetics, and mobility of bulk vacancies, motivated by interest in their use as oxygen conductors for solid oxide fuel cells (SOFCs) and related applications.[17] The surface oxygen chemistry of $A(III)B(III)O_3$ perovskites is less widely explored with DFT. Most studies use either the local density (LDA) or the generalized gradient (GGA) approximations coupled with supercell, slab models. The (100) terminations are commonly found to be the most stable, and vacancies and oxygen adsorbates at both the $AO(100)$ and $BO_2(100)$ terminations have received attention. Lee et al.[18] reported that oxygen vacancy formation energies at the (100) $BO_2$ termination of $LaBO_3$, B = Mn, Fe, Co, Ni, were lower than in the bulk. Mastrikov et al.[19] and Kotomin et al.[19,20] compared the stability of various surface terminations of $LaMnO_3$ and concluded the $MnO_2(100)$ surface is the most stable under SOFC conditions; Mastrikov et al.[21] further showed that $O_2$ dissociates with modest barrier on this termination and that dissociated O readily inserts into surface vacancies. Others have considered O and $O_2$ adsorption on both terminations,[22−25] including the dynamics of $O_2$ dissociation with kinetic Monte Carlo.[26] Thus can DFT provide insights regarding surface oxygen exchange by a variety of lattice and extralattice routes.

In this paper, we describe results from a combined experimental and computational investigation of the NO oxidation activities and oxygen exchange chemistries of a series of $La_{1-x}Sr_xCoO_3$ perovskite catalysts ($x$ = 0, 0.1, and 0.3). Oxygen exchange was characterized using Isothermal Isotope Exchange (IIE) and Temperature Programmed Isotope Exchange (TPIE) experiments using labeled $^{18}O_2$. The results were correlated with the NO oxidation rates and results from NO temperature programmed desorption (TPD) experiments. The experimental results are complemented by DFT calculations of oxygen vacancies and extra-lattice oxygen on the (100) surfaces of $LaCoO_3$ and $La_{1-x}Sr_xCoO_3$. We find that Sr doping enhances the NO oxidation activities and exchange rates, and oxygen exchange occurs through two channels at distinctly different temperatures. We also propose pathways through which oxygen exchange occurs.

## 2. EXPERIMENTAL SECTION

**2.1. Catalyst Preparation.** The $La_{1-x}Sr_xCoO_3$ catalysts were prepared using a citrate method. Appropriate amounts of $La(NO_3)_3{\cdot}6H_2O$, $Sr(NO_3)_2$, and $Co(NO_3)_2{\cdot}6H_2O$ were dissolved in distilled water. Citric acid monohydrate was added to the mixture in 10 wt % excess to ensure complete complexation of the metal ions. The solution was stirred at room temperature for 1 h and then heated to 80 °C with continuous stirring. Water was evaporated at 80 °C until the solution became a viscous gel. The gel was then dried overnight at 90 °C. The resulting spongy material was crushed and then calcined in static air at 700 °C for 5 h.

**2.2. Catalysts Characterization.** The Brunauer−Emmett−Teller (BET) surface areas were determined via $N_2$ physisorption using a Micromeritics ASAP 2020 analyzer. Prior to the measurements, the catalysts were degassed at 300 °C under vacuum. X-ray diffraction (XRD) analysis was performed using a Rigaku Miniflex Diffractometer with Cu $K_\alpha$ radiation and a Ni filter ($\lambda$ = 1.540 Å). Diffraction patterns were collected in the $2\theta$ range of 10−80°, at a rate of 5°/min with a 0.02 step size. Phase identification was achieved by comparison with the JCPDS files. Pulse chemisorption experiments were performed using a Micromeritics AutoChem II 2920 analyzer equipped with a thermal conductivity detector and a Pfeiffer Thermostar mass spectrometer. Prior to analysis, the catalysts were pretreated in 1% $O_2$/He for 1 h at 500 °C. After cooling to room temperature, the catalysts were degassed in flowing He for 30 min. The catalysts were then repeatedly dosed with 0.5 mL of 2% NO/He until saturation was achieved. The NO- and $NO_2$-temperature programmed desorption (TPD) experiments were also performed using the Micro-


dx.doi.org/10.1021/cs400522r | ACS Catal. 2013, 3, 2719−2728

meritics Autochem II 2920 analyzer. The catalysts were pretreated with 1% $^{18}O_2$/He or 1% $^{16}O_2$/He for 1 h at 500 °C, cooled to room temperature, then degassed in flowing He for 30 min. The catalysts were repeatedly dosed with 0.5 mL of 2% NO/He until the surface became saturated. After saturation was achieved, weakly adsorbed NO was purged from the surface with flowing He for 30 min. The reactor effluent was monitored using a mass spectrometer while the temperature was increased from room temperature (RT) to 500 °C at a heating rate of 10 °C/min.

**2.3. NO Oxidation Rate Measurements.** The NO oxidation rate measurements were performed in a quartz microreactor. Between 20 and 30 mg of catalyst was loaded into the tubular quartz microreactor (i.d. 6 mm). The rate measurements were carried out under differential conditions by restricting the NO conversion to less than 15%. The NO concentration was measured using an infrared NO analyzer (Horiba, AIA 210). The NO oxidation rates were measured by randomly varying the temperature between 190 and 250 °C while maintaining the feed composition at 270 ppm NO, 0 or 254 ppm $NO_2$, 10% $O_2$, and balanced $N_2$ and the total flow rate at 320 mL/min.

**2.4. Isotopic Oxygen Exchange.** The TPIE and IIE experiments were performed using a Micromeritics AutoChem II 2920 equipped with a Pfeiffer Thermostar mass spectrometer. The U-tube microreactor was loaded with 25 mg of catalyst. The mass spectrometer was used to monitor the oxygen species: $^{16}O_2$ ($m/e$ = 32), $^{16}O^{18}O$ (34), and $^{18}O_2$ (36). Prior to the TPIE experiments, the catalysts were pretreated at 500 °C for 1 h in flowing mixture of 1% $^{18}O_2$/He to pre-exchange the surface oxygen and some of bulk oxygen with $^{18}O$. After cooling to RT, the samples were degassed in He for 30 min. During the TPIE experiments, the samples were heated to 700 °C at a rate of 10 °C/min in flowing 10% $^{16}O_2$/He.

During the IIE experiments, the samples were pretreated in 10% $^{16}O_2$/He at 500 °C for 1 h. At 500 or 250 °C the samples were degassed in He for 30 min. The gas was then switched to a mixture containing 1% $^{18}O_2$ in He flowing at 10 mL/min, and the effluent was monitored using a mass spectrometer for 30 or 60 min.

**2.5. Computational Methods.** Spin-polarized, plane-wave supercell DFT calculations were done in VASP[28] using the projector augmented wave (PAW) treatment of the core electronic states and the PW91 variant of the generalized gradient approximation (GGA).[29] The cobalt ion is paramagnetic, and all calculations were initialized in the ferromagnetic state. Test calculations show that the net magnetism has a minor influence on computed results. We used a plane wave cut off energy of 400 eV and converged forces on each atom to 0.05 eV/Å$^2$. We sampled the first Brillouin zone using 6 × 6 × 6 and 2 × 2 × 1 k-point meshes in the bulk and slab calculation, respectively. The $LaCoO_3$ lattice constant within these approximations was calculated to be 3.824 Å, close to the experimental value of 3.805 Å.[30] The lattice constant is held fixed in all subsequent calculations. All slab calculations include a dipole correction to correct for asymmetry in the stoichiometric slabs.

## 3. RESULTS

**3.1. Microstructural Properties.** Surface areas for the $La_{1-x}Sr_xCoO_3$ materials were similar and are listed in Table 1. Diffraction patterns for the $La_{1-x}Sr_xCoO_3$ catalysts are illustrated in Figure 1 and indicated the presence of the rhombohedral distorted perovskite structure (JCDPDF 00-036-1392).[31] This result suggested that the calcination conditions were sufficient to produce well-crystallized perovskite structures. The $LaCoO_3$ and $La_{0.9}Sr_{0.1}CoO_3$ were phase pure perovskites, but the diffraction pattern for the $La_{0.7}Sr_{0.3}CoO_3$ material contained peaks for $SrCO_3$, SrO, and $Co_3O_4$, which indicated some degree of phase segregation.

**Table 1. Physiochemical Properties of the $La_{1-x}Sr_xCoO_3$ Perovskite Catalysts**

| property | $LaCoO_3$ | $La_{0.9}Sr_{0.1}CoO_3$ | $La_{0.7}Sr_{0.3}CoO_3$ |
|---|---|---|---|
| BET surface area ($m^2/g$) | 8.1 ± 0.1 | 8.4 ± 0.1 | 8.6 ± 0.1 |
| NO uptake ($\mu mol/g_{cat}$) | 18.9 ± 0.9 | 23.1 ± 1.1 | 20.4 ± 1.0 |
| site density (sites/$m^2$ × $10^{18}$) | 1.40 | 1.65 | 1.43 |

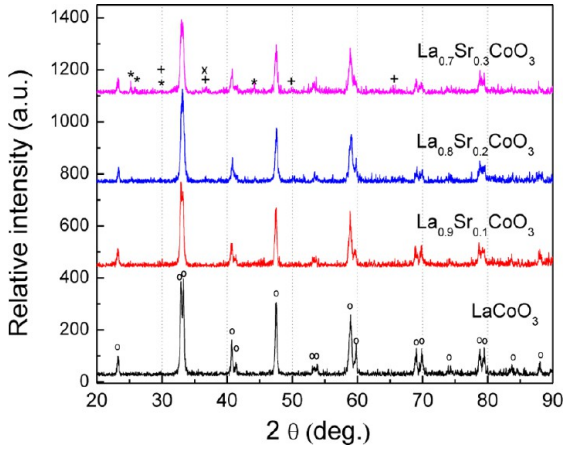


**Figure 1.** X-ray diffraction patterns for $La_{1-x}Sr_xCoO_3$; (○) Perovskite structure, (*) $SrCO_3$, (x) SrO, (+) $Co_3O_4$.

**3.2. NO Oxidation Rates.** Figure 2 illustrates NO oxidation rates for the $La_{1-x}Sr_xCoO_3$ catalysts in the absence and presence of $NO_2$ in the feed. In the absence of $NO_2$, the Sr-substituted catalysts exhibited slightly higher NO oxidation rates than $LaCoO_3$ with the $La_{0.9}Sr_{0.1}CoO_3$ catalyst being the most active. It has been reported that $NO_2$ inhibits the NO oxidation activities of Pt[27] and Pd[14] based catalysts. With $NO_2$ in the feed, NO oxidation rates for all of the $La_{1-x}Sr_xCoO_3$

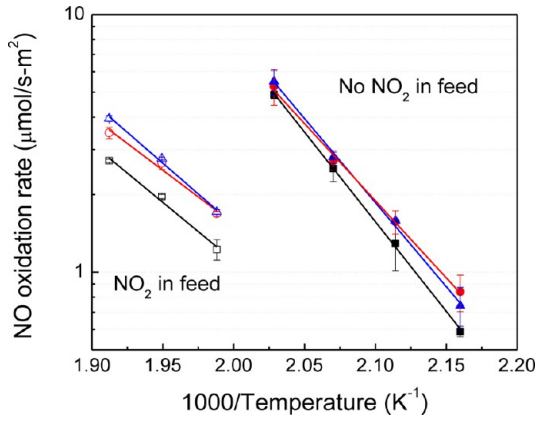


**Figure 2.** Arrhenius plots of NO oxidation rates for (■) $LaCoO_3$, (●) $La_{0.9}Sr_{0.1}CoO_3$, and (▲) $La_{0.7}Sr_{0.3}CoO_3$. Reaction conditions: 270 ppm NO, 0 or 254 ppm $NO_2$, 10% $O_2$, balanced $N_2$, total flow rate = 320 mL/min, 190−250 °C.


dx.doi.org/10.1021/cs400522r | ACS Catal. 2013, 3, 2719−2728

catalysts decreased significantly; however, rates over the $La_{0.9}Sr_{0.1}CoO_3$ and $La_{0.7}Sr_{0.3}CoO_3$ catalysts were almost 50% higher than those for the $LaCoO_3$ catalyst. These results indicate that Sr substitution reduced the extent of $NO_2$ inhibition.

**3.3. NO and $NO_2$ TPD.** The TPD spectra following NO adsorption on the $^{16}O_2$- or $^{18}O_2$-pretreated $LaCoO_3$ are shown in Figures 3 and 4. The mass spectrometer signals were taken

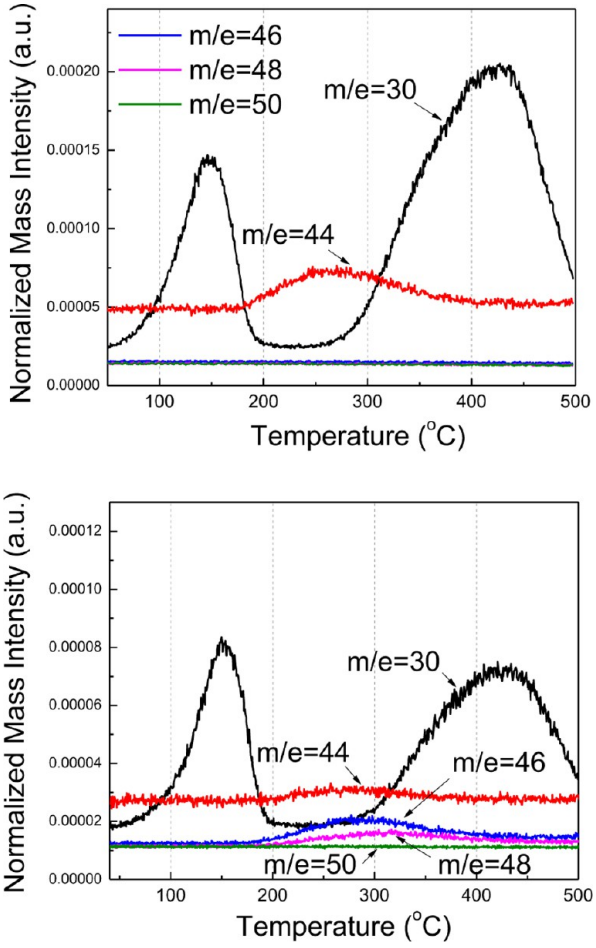


**Figure 3.** NO-TPD profiles for (top) $^{16}O_2$-pretreated $LaCoO_3$ and (bottom) $^{18}O_2$-pretreated $LaCoO_3$ as a function of temperature. Assignments for the *m/e* are provided in Table 2

to correspond to the species in Table 2. The principal $NO_x$ species desorbing from $LaCoO_3$ were NO and/or $NO_2$ at ~150 and 430 °C, and $N_2O$ at ~250 °C. The presence of $N_2O$ suggests some NO disproportionation (2 NO → $N_2O$ + O*) on the $LaCoO_3$ surface. Pretreatment with $^{18}O_2$ (Figure 4b) instead of $^{16}O_2$ (Figure 4a) resulted in a reduction in the NO/$NO_2$ and $N_2O$ peaks, and an increase in the $NO^{18}O$ and $N_2{}^{18}O$ peaks. Temperatures for the $N_2O$ and $N_2{}^{18}O$ peaks were similar. Our observation that temperatures for the NO/$NO_2$ and $NO^{18}O$ peaks were different suggests that the NO/$NO_2$ peak was dominated by NO with perhaps a shoulder for $NO_2$ on the high temperature peak. The desorption of $NO^{18}O$ and $N_2{}^{18}O$ clearly indicated the exchange of surface $^{16}O$ with $^{18}O$, the reaction of $^{18}O$ with NO and possibly the exchange of oxygen in $N_2O$.

In addition to $NO_x$ species, $O_2$ ($O_2$, $^{16}O^{18}O$, and $^{18}O_2$) desorbed from $LaCoO_3$ during the NO TPD. We believe the

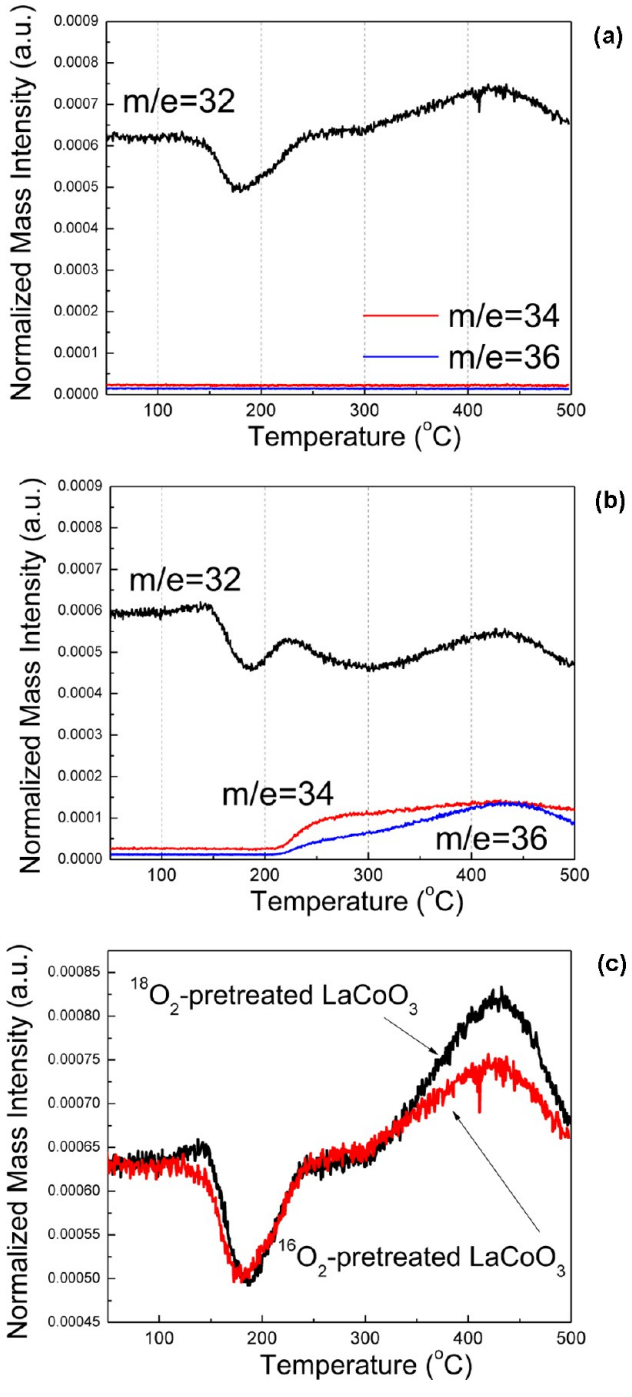


**Figure 4.** NO-TPD profiles for (a) $^{16}O_2$-pretreated $LaCoO_3$, (b) $^{18}O_2$-pretreated $LaCoO_3$, and (c) the summation of the *m/e* = 32, 34, and 36 signals for both $^{16}O_2$- and $^{18}O_2$-pretreated $LaCoO_3$ as a function of temperature. Assignments for the *m/e* are provided in Table 2.

peak for *m/e* = 32 was due to $O_2$ as opposed to $N^{18}O$ because of the presence of a peak for *m/e* = 36 at the same temperature. The desorption of $O_2$ is consistent with NO disproportionation. For both the $^{16}O_2$- (Figure 4a) and $^{18}O_2$-pretreated (Figure 4b) materials, the major $O_2$ desorption peak occurred at ~430 °C; this temperature coincides with that for the high temperature NO desorption peaks. The total $O_2$ that desorbed from $LaCoO_3$ (Figure 4c) following $^{16}O_2$-pretreatment was less than that following $^{18}O_2$-pretreatment (Figure 4c). The increase in total $O_2$ desorption on pretreatment in $^{18}O_2$ vs $^{16}O_2$ was


dx.doi.org/10.1021/cs400522r | ACS Catal. 2013, 3, 2719−2728

**Table 2. Values of *m/e* for Species Tracked Using Mass Spectrometry**

| *m/e*: | molecule | *m/e* | molecule |
|---|---|---|---|
| 28 | $N_2$ | 48 | $NO^{18}O$ |
| 30 | NO[a] | 46 | $NO_2$ |
| 32 | $N^{18}O$[b] | 50 | $N^{18}O_2$ |
| 44 | $N_2O$ | 32 | $O_2$ |
| 46 | $N_2{}^{18}O$ | 36 | $^{18}O_2$ |

[a]Major fragment from $NO_2$ and minor fragment from $NO^{18}O$. [b]Major fragment from $N^{18}O_2$ and minor fragment from $NO^{18}O$.

similar in character to the decrease in NO desorption (comparing Figures 3a and b). The basis for this correspondence and the apparent effect of $^{18}O_2$ pretreatment are not clear. Peak temperatures for total $O_2$ ($O_2$, $^{16}O^{18}O$ and $^{18}O_2$) desorption for the $^{16}O_2$- and $^{18}O_2$-pretreated $La_xSr_{1-x}CoO_3$ catalysts decreased with increasing Sr content (Figure 5). This suggested that oxygen exchange was facilitated by the presence of Sr.

$NO_2$ desorbed from the Sr-doped catalysts at approximately 390 °C; $NO_2$ desorbed from $LaCoO_3$ at a higher temperature (~430 °C). This observation is consistent with $NO_2$ desorbing more easily from the surface of Sr substituted catalysts than from $LaCoO_3$. Peak areas indicated that the amount of $N^{16}O^{18}O$ desorbing from the surface was greater for $La_{0.9}Sr_{0.1}CoO_3$ than for $La_{0.7}Sr_{0.3}CoO_3$ and $LaCoO_3$. These results are consistent with Sr substitution causing an increase in the amount of $N^{16}O^{18}O$ desorption and enhancing desorption of $NO_2$ from the surface. This could help reconcile the reduced $NO_2$ inhibition for Sr-substituted catalysts.

Results for $NO_2$ TPD from the $La_{1-x}Sr_xCoO_3$ catalysts are illustrated in Figure 6. The character of profiles for the $LaCoO_3$ catalyst was very different from that for the $La_{0.9}Sr_{0.1}CoO_3$ and $La_{0.7}Sr_{0.3}CoO_3$ catalysts with the onset of $NO_2$ desorption decreasing with increased Sr substitution. In addition, peak areas for the $La_{1-x}Sr_xCoO_3$ catalysts were lower than those for the $LaCoO_3$ catalyst.

**3.4. Isotope Oxygen Exchange.** Figure 7a illustrates changes in the normalized signals for $^{16}O^{18}O$ ($m/e$ = 34) produced by simple heteroexchange, as a function of the temperature. The $LaCoO_3$ catalyst had desorption peaks centered at ~194, ~355, and ~558 °C. Comparison with results in the literature[32] suggest that the low temperature peak was due to oxygen exchanged with surface oxygen, and the higher temperature peaks originated from oxygen exchanged with subsurface and/or grain boundary oxygen, respectively. The intensity of the highest temperature peak was much higher than that for the other peaks. With Sr substitution, the peaks shifted to lower temperatures indicating that oxygen exchange was enhanced by Sr substitution. Cobalt exhibits valencies between 2+ and 4+, while the valencies for La (3+) and Sr (2+) are fixed. The substitution of La by Sr could produce oxygen vacancies in the lattice to maintain charge balance. Trends for $^{18}O_2$ ($m/e$ = 36) desorption were similar to those for $^{16}O^{18}O$ and are illustrated in Figure 7b. The desorption of $^{18}O_2$ indicated multiple heteroexchange. The $^{18}O_2$ desorption peak areas were much smaller than those for the $^{16}O^{18}O$ peaks, indicating that the extent of multiple heteroexchange was much lower than that for simple heteroexchange. This result is consistent with previous reports.[31] Note that $^{18}O_2$ started desorbing from the $La_{1-x}Sr_xCoO_3$ catalysts at temperatures that were lower than those for $^{16}O^{18}O$ desorption, suggesting that

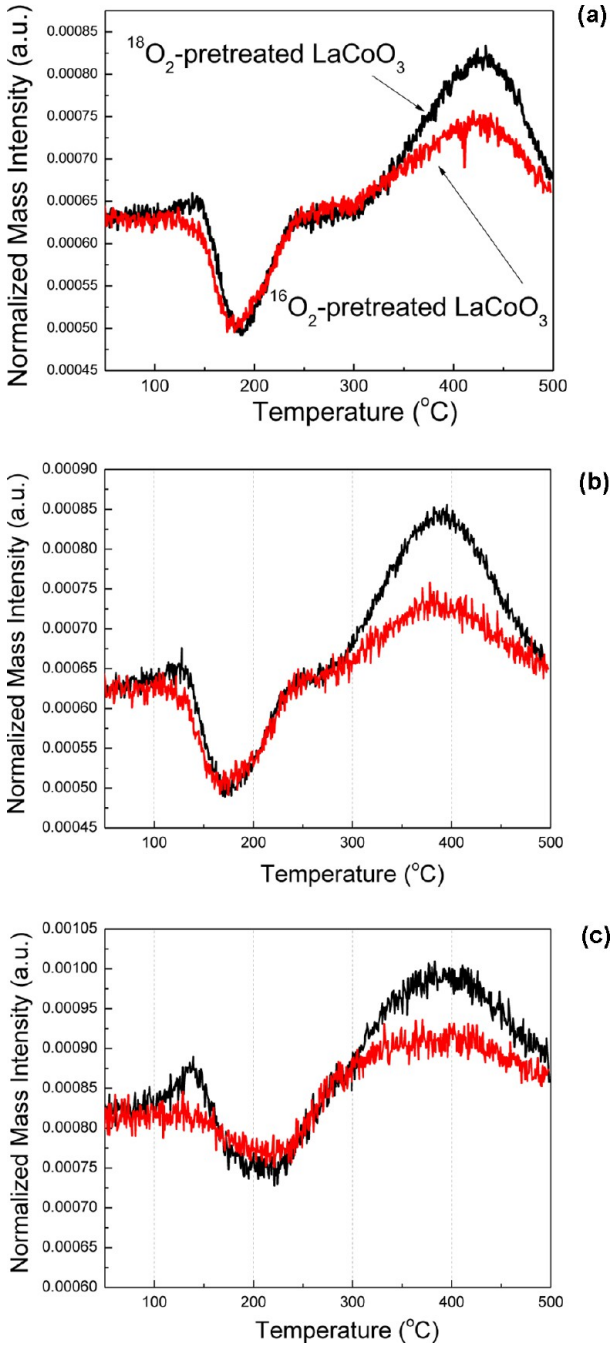


**Figure 5.** Summation of NO-TPD profile for $m/e$ = 32, 34, and 36 signals for (a) $LaCoO_3$, (b) $La_{0.9}Sr_{0.1}CoO_3$ and (c) $La_{0.7}Sr_{0.3}CoO_3$ as a function of temperature. Assignments for the $m/e$ are provided in Table 2

the multiple heteroexchange was more facile than simple heteroexchange.

Results from the IIE experiments at 500 °C are illustrated in Figure 8. The $^{16}O_2$ ($m/e$ = 32) and $^{16}O^{18}O$ ($m/e$ = 34) signals, which correspond to multiple and simple heteroexchange, respectively, increased rapidly and then slowly decreased, while the $^{18}O_2$ signal ($m/e$ = 36) gradually increased as shown in Figure 8a. The sum of signals for $^{16}O_2$, $^{16}O^{18}O$, and $^{18}O_2$ increased rapidly after ~2.5 min (due to a time lag on introduction of $^{18}O_2$) then reached a relatively constant value, suggesting that there was no net oxygen consumed or produced during IIE. The onset of $^{16}O_2$ desorption occurred at a lower


dx.doi.org/10.1021/cs400522r | ACS Catal. 2013, 3, 2719−2728

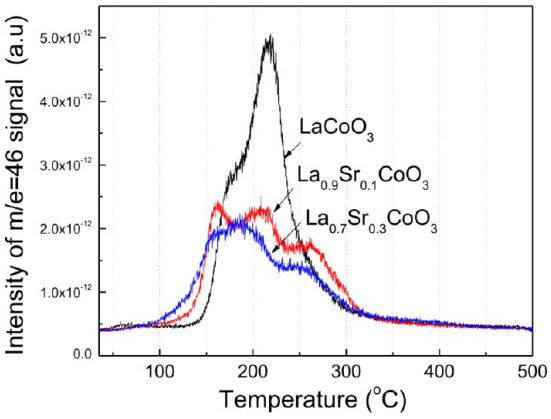


**Figure 6.** $NO_2$-TPD profiles for $La_{1-x}Sr_xCoO_3$ catalysts as a function of temperature.

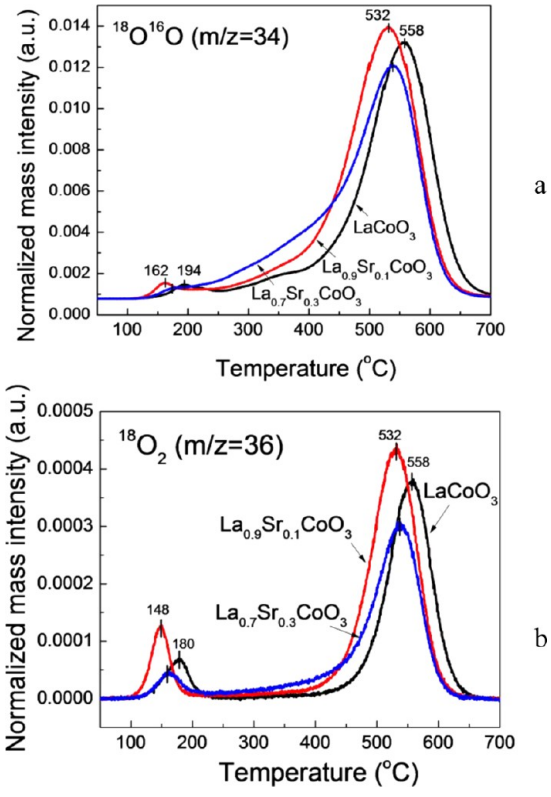


**Figure 7.** Changes in the (a) $m/e$ = 34 ($^{18}O^{16}O$) and (b) 36 ($^{18}O_2$) signals for $La_{1-x}Sr_xCoO_3$ catalysts pretreated with 1% $^{18}O_2$ at 500 °C for 1 h as a function of temperature.

temperature than that for $^{16}O^{18}O$, indicating that multiple heteroexchange was easier than simple heteroexchange. This is consistent with the TPIE results. Similar trends were observed for the $La_{0.9}Sr_{0.1}CoO_3$ and $La_{0.7}Sr_{0.3}CoO_3$ catalysts (not shown here). The $^{18}O_2$ profiles for the $La_xSr_{1-x}CoO_3$ catalysts are illustrated in Figure 8b. Given that the oxygen exchange rates are proportional to the slope, exchange rates for $La_{0.9}Sr_{0.1}CoO_3$ and $La_{0.7}Sr_{0.3}CoO_3$ catalysts were higher than that for the $LaCoO_3$ catalyst. Intensities for $m/e$ = 32, 34, and 36 measured during IIE experiments at 250 °C are shown in Figure 9. Based on the TPIE results, gaseous oxygen only exchanged with surface oxygen at this temperature. The oxygen exchange reaction seemed to reach steady state after approximately 30

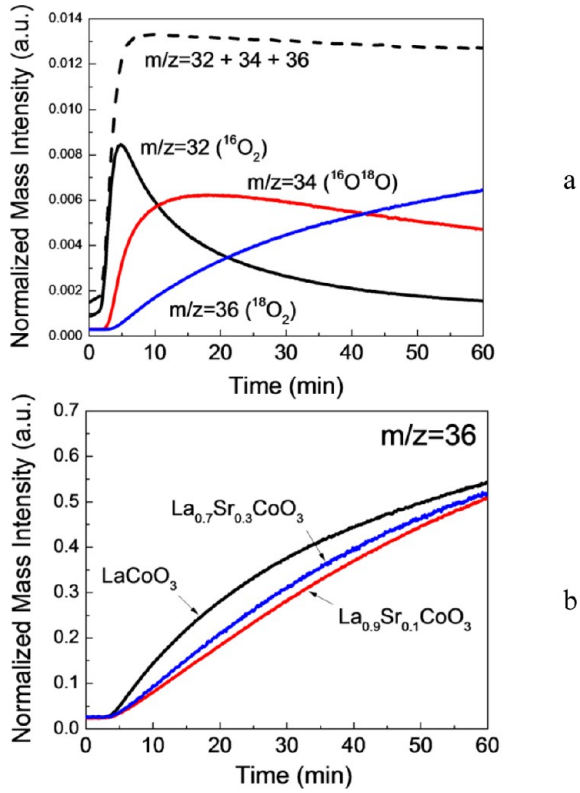


**Figure 8.** Changes in the $m/e$ = 32, 34, and 36 signals for (a) $LaCoO_3$ and (b) 36 for $La_{1-x}Sr_xCoO_3$ catalysts as a function of time from IIE at 500 °C.

min of exposure to $^{18}O_2$, while oxygen exchange rates decreased gradually even after 60 min at 500 °C.

The steady-state oxygen exchange rates were calculated from the molar flow rate and fractions of the various species and are listed in Table 3. The simple heteroexchange rate increased with Sr-substitution leading to increased total oxygen exchange. The NO oxidation rates at 250 °C also increased with Sr-substitution.

**3.5. DFT Models of O on Perovskite.** The experiments above show that oxygen readily exchanges with the perovskite material at temperatures relevant to NO oxidation, and that NO oxidation is facile on these materials. We used DFT calculations to characterize oxygen adsorption and exchange on the undoped and doped perovskite via

$$\frac{1}{2}O_2 + * \rightarrow O* \quad (7)$$

Unlike metals, the "active site" of exchange in an oxide could involve surface vacancies or extra-lattice species. We explore both possibilities using a supercell, slab model of the $LaCoO_3$ perovskite terminated upon the most common, (100) facet of the material. Along the (100) direction the perovskite structure consists of alternating layers of LaO and $CoO_2$ stoichiometries. To consider behavior on both surfaces, we construct a six layer stoichiometric slab with LaO and $CoO_2$ terminations on opposite sides, shown in Figure 10, and apply dipole corrections to minimize the effect of electronic dipoles on the energy results. Slabs are separated by a vacuum spacing of 15 Å, chosen by testing the variation in total energy with vacuum distance and the decay of the local potential away from the surfaces. Figure 10 compares the structures of the unrelaxed


dx.doi.org/10.1021/cs400522r | ACS Catal. 2013, 3, 2719−2728

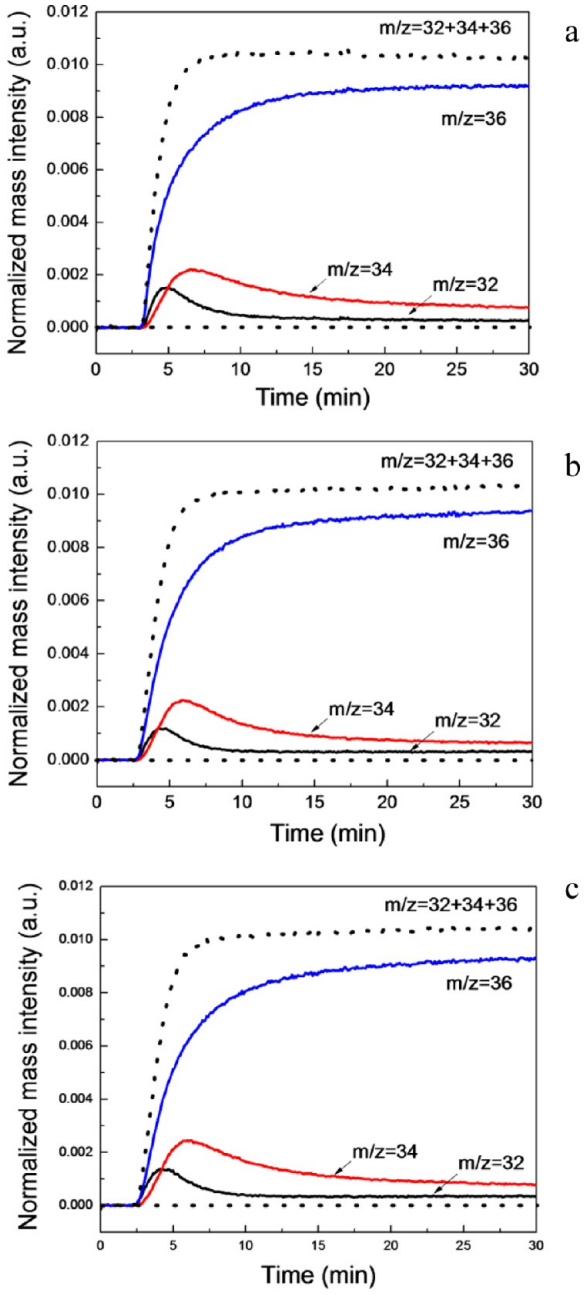


**Figure 9.** Changes in the $m/e$ = 32, 34, and 36 signals for (a) $LaCoO_3$, (b) $La_{0.9}Sr_{0.1}CoO_3$, and (c) $La_{0.7}Sr_{0.3}CoO_3$ as a function of time from IIE at 250 °C.

**Table 3. Oxygen Exchange Rates and Amounts for $La_{1-x}Sr_xCoO_3$ Catalysts**

| | oxygen exchange rate ($\mu$mol/m$^2$ s × 10$^{-3}$)[a] | | oxygen exchanged ($\mu$mol/m$^2$)[b] | |
|---|---|---|---|---|
| catalyst | simple | multiple | simple | multiple |
| $LaCoO_3$ | 17.2 ± 0.9 | 4.3 ± 0.2 | 57.8 ± 2.9 | 19.9 ± 1.0 |
| $La_{0.9}Sr_{0.1}CoO_3$ | 21.3 ± 1.1 | 3.3 ± 0.2 | 68.3 ± 3.4 | 19.0 ± 1.0 |
| $La_{0.7}Sr_{0.3}CoO_3$ | 22.3 ± 1.1 | 3.1 ± 0.1 | 65.2 ± 3.3 | 21.9 ± 1.1 |

[a]Calculated from the molar flow rate multiplied by fraction of $m/e$ = 34 (simple) or 32 (multiple) after 30 min time on stream. [b]Calculated from peak area for $m/e$ = 34 (simple) and 32 (multiple), respectively.

cubic slab and an unconstrained relaxed slab. As noted previously,[18,33] the $CoO_6$ octahedra twist and Jahn−Teller distort, such that the planar symmetry of the O layers is broken. Most evident is the upward relaxation of O ions at the LaO(100) termination. The cation relaxations are less pronounced.

We computed vacancy formation energies for oxygen removed from each layer of the slab in turn as defined in eq 7. The results in Figure 11 show that the vacancy formation energy steadily decreases from the LaO termination (4.07 eV) to the $CoO_2$ termination (1.74 eV). The vacancy energy at the center of the slab model is close to the value we compute separately for the bulk oxide in a 2 × 2 × 2 supercell (2.98 eV). For comparison, Lee et al. report a bulk vacancy energy of 2.6 eV, using a Hubbard U-corrected GGA model and empirically corrected molecular $O_2$ energy,[18] and further report a significant decrease in vacancy formation energy at the $CoO_2$ termination. Mizusaki et al.[34] used thermogravimetric analysis and the van't Hoff relationship to estimate a bulk vacancy energy of 2.2 eV in the dilute limit, increasing with vacancy density. Based on these comparisons, the GGA model used here tends to exaggerate absolute vacancy formation energies by approximately 0.4 to 0.8 eV.

We next consider the substitution of a single Sr for La in the slab, corresponding to a dilute doping level of 5.5%. The slab with the Sr dopant substituted for a La ion in the LaO termination is 0.59 eV lower in energy than Sr in the first subsurface layer and 0.81 eV lower in energy than Sr subsurface to the $CoO_2$ termination. Sr thus strongly prefers to segregate toward the LaO termination. The $Sr^{2+}$ ion is 8% larger than $La^{3+}$, and this size difference likely influences this segregation tendency. The diamonds in Figure 11 show the effect of a Sr dopant in the top LaO layer on vacancy formation energies throughout the slab. Sr generally lowers the energy to create a vacancy, and the effect is strongest in the $CoO_2$ layer immediately subsurface of the dopant. This stabilization effect dies off with distance into the slab on the LaO layers. It persists to longer range on the $CoO_2$ layers, and introduces the largest destabilization of vacancies on the opposite, $CoO_2$ termination. When we place a Sr dopant subsurface to the $CoO_2$ termination, the vacancy formation energy in the $CoO_2$ termination increases by 0.05 eV.

These results show that vacancies in the $CoO_2$ termination are generally less energetically costly than in at the LaO termination, suggesting that the former is relevant to oxygen exchange. Extra-lattice oxygen could as well play a role in oxygen exchange, as is commonly observed in the catalytically active rutile oxides like $RuO_2$.[35] We explored adsorption of extra-lattice O and $O_2$ on both the $CoO_2$ and the LaO terminations. Co ions on the $CoO_2$ termination are coordinatively unsaturated relative to the bulk. Molecular oxygen binds to this termination atop Co and tilted away from the surface, with a modest binding energy of −0.38 eV. Atomic oxygen binding is endothermic relative to 1/2 $O_2$. A Sr dopant subsurface to the $CoO_2$ further reduces these adsorption energies.

In contrast, we find that both atomic and molecular oxygen bind quite strongly to the LaO termination. Figure 12a and b shows results for atomic O. The preferred O binding site bridges two La ions, in the location a next layer of O ions would occupy. The binding energy computed according to eq 2 is −1.66 eV. O also adsorbs atop a surface O with an O−O bond distance of 1.49 Å, consistent with that expected for a peroxide anion. The binding energy relative to the same 1/2 $O_2$ reference is a much more modest −0.40 eV. Figure 12c and


dx.doi.org/10.1021/cs400522r | ACS Catal. 2013, 3, 2719−2728

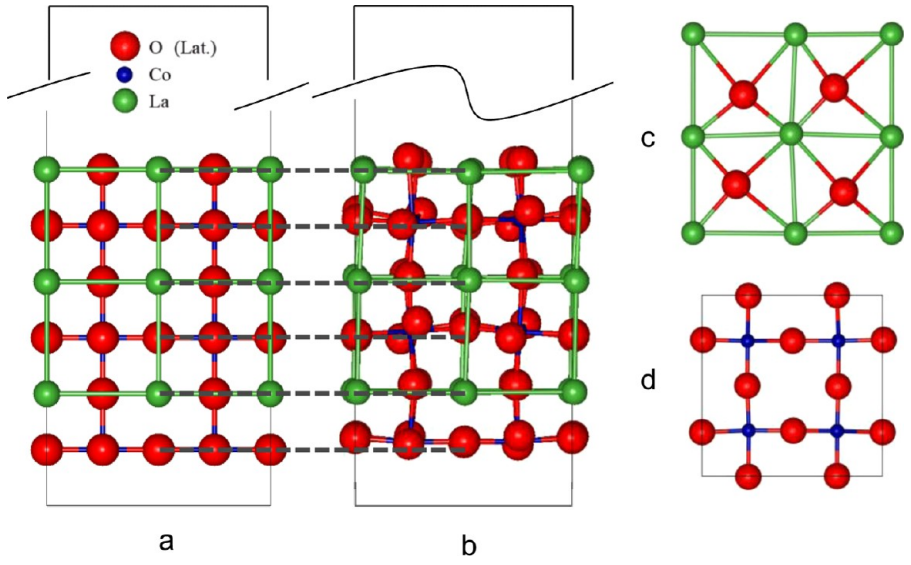


**Figure 10.** (a) Side-view of unrelaxed $LaCoO_3$ slab. (b) Side-view of relaxed $LaCoO_3$ slab, showing distortions about $CoO_6$ octahedra. (c) Top view of relaxed LaO(100) termination. (d) Top view of relaxed $CoO_2$(100) termination.

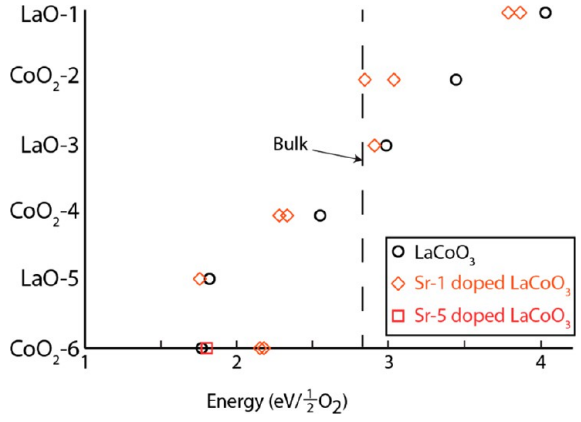


**Figure 11.** (circles) O vacancy formation energies as a function of slab layer. (diamonds) O vacancy formation energies in a slab Sr-doped in the LaO layer. Two diamonds per layer represent two symmetry-distinct vacancy sites. (square) O vacancy formation energy with Sr dopant subsurface to $CoO_2$ termination. (line) Bulk vacancy formation energy.

d shows results for molecular $O_2$ adsorption. $O_2$ prefers to associate with surface La ions; the most favorable adsorption site is parallel to the surface and spanning two La−La bridge sites, shown in Figure 12c and with a binding energy of −2 eV/$O_2$. The optimized O−O distance is similarly 1.49 Å, reflecting significant charge transfer to the adsorbate. $O_2$ also adsorbs near a single La ion, shown in Figure 12d, with a more modest −1.73 eV/$O_2$ binding energy. A Sr dopant in the LaO termination repels these oxygen adsorbates. We find no stable atomic or molecular $O_2$ adsorption sites involving direct participation of a surface Sr dopant; all the adsorption sites shown in Figure 12 become unstable with a Sr dopant substituted for La "A." Further, substitutional doping at site "B" weakens all adsorbates. Site preferences are unchanged, but binding energies decrease to −1.03 eV/1/2$O_2$, −0.02 eV/1/2$O_2$, −1.06 eV/$O_2$, and −1.40 eV/$O_2$, respectively.

Using these results we can compute $O_2$ dissociation energies for adsorbates on the LaO termination

$$O_2^* \rightarrow 2O^* \quad (8)$$

Dissociation from the most favored $O_2$ site to two infinitely separated O sites is exothermic by −1.28 eV on the undoped surface; using the analogous Sr doped references decreases this to −0.63 eV. Both the undoped and the doped surfaces adsorb and likely dissociate $O_2$.

**3.6. Discussion.** The results of the TPIE experiments indicate isotope exchange between dosed oxygen and oxygen intrinsic to the perovskite catalyst. We used these results to estimate oxygen desorption energies. We assume second-order desorption and integrated the Polanyi−Wigner[36] relationship:

$$\frac{r_d}{B_h} = \frac{d\theta}{dT} = \frac{\theta^n A}{B_h} e^{-E_a/k_b T}$$

We use a heating rate ($B_h$) of 10 °C min$^{-1}$, assume a constant prefactor ($A$) of $10^{13}$ s$^{-1}$, and vary the desorption energy $E_{des}$ until the experimentally observed rate maxima shown in Figure 7b is reproduced. By this analysis, desorption maxima in the undoped perovskite at 180 and 558 °C correspond to desorption energies of 0.51 and 1.65 eV, respectively. Peaks shift down in temperature to 162 and 532 °C in the 10% Sr-doped perovskite, corresponding to desorption energies of 0.46 and 1.57 eV. Sr doping thus lowers desorption energies on the order of 0.05 eV.

The TPIE experiments involved dosing and subsequent desorption of $O_2$. Figure 13 compares the various computed desorption processes that incorporate or liberate $O_2$, including pathways that create surface vacancies and that involve extra-lattice oxygen. While the absolute energies are subject to the GGA error, relative comparisons can be made. From the first column of the figure, oxygen divacancies on the LaO termination are clearly too high in energy to participate in oxygen exchange—GGA desorption energies approach 8 eV. Oxygen divacancies on the $CoO_2$ termination are half as high in energy and could well contribute to the higher energy desorption feature as well as to isotope exchange, since they involve creation and destruction of two vacancies. From the last column of the figure, oxygen isotope exchange could also occur on the LaO termination via an extra-lattice oxygen mechanism.


dx.doi.org/10.1021/cs400522r | ACS Catal. 2013, 3, 2719−2728

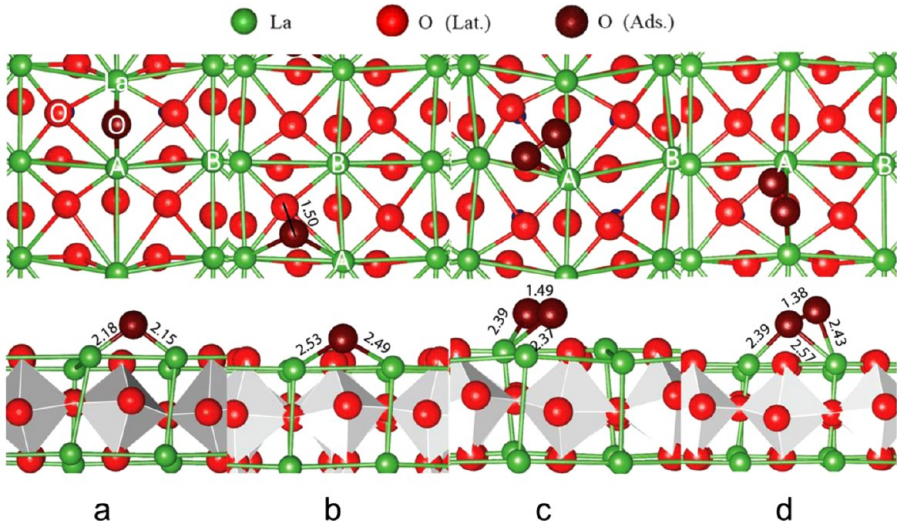


**Figure 12.** Top and side views are shown for the most stable adsorbate positions on the LaO (100) termination in this study. La–La bridge (a), O–atop (b), La–La bridge bidentate (c), and La–La bridge $O_2$ (d). Possible dopant positions are noted in each figure by A and B corresponding to first and second neighbor positions of Sr respectively.

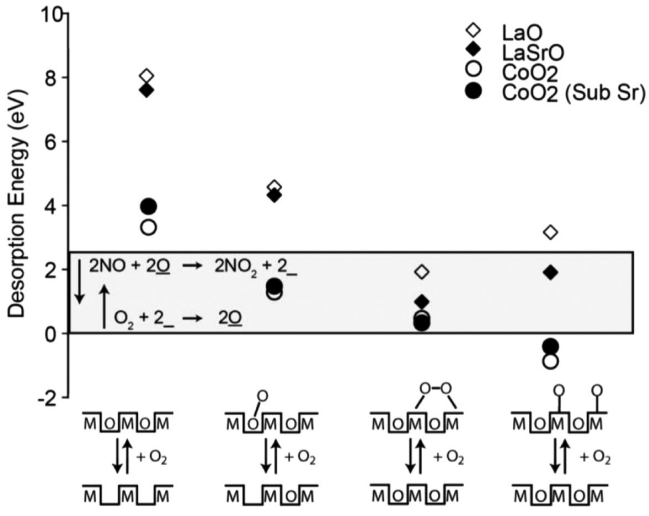


**Figure 13.** Comparison of DFT-computed surface oxygen exchange processes. Desorption energy normalized to one $O_2$ molecule in each column. The window represents the GGA-computed range of exothermic $O_2$ dissociative adsorption and NO oxidation to $NO_2$.

Sr doping lowers the energy of this process, consistent with the lower-temperature exchange observed during TPIE on the doped sample. The middle two columns of the figure correspond to molecular $O_2$ desorption/adsorption processes that do not break O–O bonds and thus would not contribute to isotopic scrambling. These too can occur through a vacancy-mediated process on the $CoO_2$ termination and through molecular adsorption on either termination; such processes may well contribute to the low temperature desorption feature observed in the TPIE experiments. From these comparisons it appears likely that oxygen exchange is possible through multiple mechanisms even on the simple (100) terminations of the perovskite.

These results can be used to reconcile the NO oxidation activities. The most commonly proposed NO oxidation mechanism on metals involves dissociative adsorption of $O_2$ and combination of adsorbed O with NO

$$O_2 + 2 \leftrightarrow 2O^* \quad (9)$$

$$NO^* + O^* \leftrightarrow NO_2^* \rightarrow NO_2 \quad (10)$$

The O–NO bond is quite weak; for the second step to proceed to the $NO_2$ product, the O* bond that is broken must also be weak enough to be compensated by the newly formed O–NO bond. Figure 13 shows the GGA-computed O desorption energy window consistent with exothermic reactions 9 and 10. We find that the $CoO_2$ termination vacancies and LaO extra-lattice O are candidate sites for NO oxidation to occur on the surface. Furthermore, we again observe Sr dopants destabilizing extra-lattice oxygen bringing them within the NO oxidation window.

## 4. CONCLUSIONS

This paper describes the effect of Sr substitution on the performance of $La_{1-x}Sr_xCoO_3$ catalysts for NO oxidation and key characteristics for these materials. The Sr-substituted catalysts exhibited higher NO oxidation rates than $LaCoO_3$. Based on NO- and $NO_2$-TPD results, Sr substitution decreased the amount of $NO_2$ adsorption and enhanced $NO_2$ desorption. Results from the TPIE and IIE experiments indicated that the principal oxygen exchange mechanism for $La_{1-x}Sr_xCoO_3$ was the simple heteroexchange and that Sr substitution enhanced the total oxygen exchange capacity. The DFT calculations indicated that lattice oxygen was bound strongly and that weakly bound extralattice oxygen was likely available for simple-heteroexchange. The DFT also indicated that the addition of Sr destabilized the extralattice oxygen in agreement with TPIE peak shifts as well as the oxygen exchange experiments. There was good correlation between the simple heteroexchange and NO oxidation rates for the $La_{1-x}Sr_xCoO_3$ catalysts. The results suggest that Sr substitution increases the NO oxidation rate as a consequence of enhancing oxygen activity.

## AUTHOR INFORMATION

### Corresponding Authors

*E-mail: chang.h.kim@gm.com (C.H.K.).
*E-mail: wschneider@nd.edu (W.F.S.).
*E-mail: ltt@umich.edu (L.T.T.).

## Notes

The authors declare no competing financial interest.

## ■ ACKNOWLEDGMENTS

Support from National Science Foundation GOALI program under CBET grants 0967434 and 0967466 is gratefully acknowledged.

## ■ REFERENCES

(1) (a) Weiss, M. A.; Heywood, J. B.; Drake, E. M.; Schafer, A.; AuYeung, F. F. MIT 2000 Energy Laboratory Report EL 00-003; MIT: Cambridge, MA, 2000; (b) Sullivan, J. L.; Baker, R. E.; Boyer, B. A.; Hammerle, R. H.; Kenney, T. E.; Muniz, L.; Wallington, T. J. *Environ. Sci. Technol.* **2004**, *38* (12), 3217−3223.
(2) U.S. DRIVE, Advanced Combustion and Emission Control Roadmap. U.S. Department of Energy.
(3) Kim, C.; Qi, G.; Dahlberg, K.; Li, W. *Science* **2010**, 1624−1627.
(4) Takahasi, N.; Shinjoh, H.; Iijima, T.; Suzuki, T.; Yamazaki, K.; Yokota, K.; Suzuki, H.; Miyoshi, N.; Matsumoto, S.-i.; Tanizawa, T.; Tanaka, T.; Tateishi, S.-s.; Kasahara, K. *Catal. Today* **1996**, *27*, 63−69.
(5) Heck, R. M.; Farrauto, R. J. *Appl. Catal., A* **2001**, *221* (1−2), 443−457.
(6) (a) Bourges, P.; Lunati, S.; Mabilon, G. $N_2O$ and $NO_2$ formation during NO reduction on precious metal catalysts. In *Proceedings of the Fourth International Symposium, Catalysis and Automotive Pollution Control IV*, Brussels, Belgium, April 9−11, 1997; Elsevier: New York, 1998; Vol. *116*, pp 213−222. (b) Despres, J.; Elsener, M.; Koebel, M.; Krocher, O.; Schnyder, B.; Wokaun, A. *Appl. Catal., B* **2004**, *50* (2), 73−82.
(7) (a) Yung, M.; Holmgreen, E.; Ozkan, U. *J. Catal.* **2007**, *247* (2), 356−367. (b) Irfan, M.; Goo, J.; Kim, S. *Appl. Catal., B* **2008**, *78* (3−4), 267−274. (c) Wen, Y.; Zhang, C.; He, H.; Yu, Y.; Teraoka, Y. *Catal. Today* **2007**, *126* (3−4), 400−405.
(8) Idriss, H.; Barteau, M. A. *Adv. Catal.* **2000**, *45*, 261.
(9) Mars, P.; Van Krevelen, D. W. *Chem. Eng. Sci.* **1954**, *3*, 41−59.
(10) (a) Bialobok, B.; Trawczynski, J.; Mista, W.; Zawadzki, M. *Appl. Catal., B* **2007**, *72* (3−4), 395−403. (b) Chien, C.; Shi, J.; Huang, T. *Ind. Eng. Chem. Res.* **1997**, *36* (5), 1544−1551. (c) Dow, W.; Huang, T. *J. Catal.* **1996**, *160* (2), 171−182. (d) Islam, M.; Cherry, M.; Winch, L. *J. Chem. Soc., Faraday Trans.* **1996**, *92* (3), 479−482.
(11) (a) Tanaka, H.; Misono, M. *Curr. Opin. Solid State Mater. Sci.* **2001**, *5* (5), 381−387. (b) Seiyama, T.; Yamazoe, N.; Eguchi, K. *Ind. Eng. Chem. Prod. Res. Dev.* **1985**, *24* (1), 19−27.
(12) (a) Over, H. *Science* **2000**, *287* (5457), 1474−1476. (b) Over, H. *Chem. Rev.* **2012**, *112* (6), 3356−426.
(13) Jelic, J.; Reuter, K.; Meyer, R. *ChemCatChem* **2010**, *2* (6), 658−660.
(14) Weiss, B. M.; Iglesia, E. *J. Catal.* **2010**, *272* (1), 74−81.
(15) Boreskov, G. K. *Adv. Catal.* **1965**, *15*, 285−339.
(16) Winter, E. R. S. *Adv. Catal.* **1958**, *10*, 196−241.
(17) (a) Kummer, J. T. *J. Phys. Chem.* **1986**, *90*, 4747−4752. (b) Crumlin, E. J.; Mutoro, E.; Liu, Z.; Grass, M. E.; Biegalski, M. D.; Lee, Y.-L.; Morgan, D.; Christen, H. M.; Bluhm, H.; Shao-Horn, Y. *Energy Env. Sci.* **2012**, *5* (3), 6081.
(18) Lee, Y.-L.; Kleis, J.; Rossmeisl, J.; Morgan, D. *Phys. Rev. B* **2009**, *80* (22), 224101.
(19) Mastrikov, Y. A.; Heifets, E.; Kotomin, E. A.; Maier, J. *Surf. Sci.* **2009**, *603* (2), 326−335.
(20) Kotomin, E. A.; Mastrikov, Y. A.; Heifets, E.; Maier, J. *Phys. Chem. Chem. Phys.* **2008**, *10* (31), 4644.
(21) Mastrikov, Y.; Merkle, R.; Heifets, E. *J. Catal.* **2010**.
(22) Piskunov, S.; Heifets, E.; Jacob, T.; Kotomin, E.; Ellis, D.; Spohr, E., *Phys. Rev. B* 2008, *78* (12).
(23) Piskunov, S.; Jacob, T.; Spohr, E. *Phys. Rev. B* **2011**, *83* (7), 121406.
(24) Choi, Y.; Lin, M.; Liu, M. *Angew. Chem., Int. Ed.* **2007**, *46*, 7214−7219.
(25) Pilania, G.; Ramprasad, R. *Surf. Sci.* **2010**, *604* (21−22), 1889−1893.
(26) Pilania, G.; Gao, P.-X.; Ramprasad, R. *J. Phys. Chem. C* **2012**, *116* (50), 26349−26357.
(27) (a) Mulla, S. S.; Chen, N.; Delgass, W. N.; Epling, W. S.; Ribeiro, F. H. *Catal. Lett.* **2005**, *100* (3 - 4), 267. (b) Mulla, S. S.; Chen, N.; Cumaranatunge, L.; Blau, G. E.; Zemlyanov, D.; Delgass, W. N.; Epling, W. S.; Ribeiro, F. H. *J. Catal.* **2006**, *241*, 389−399. (c) Weiss, B. M.; Iglesia, E. *J. Phys. Chem. C* **2009**, *113* (30), 13331−13340. (d) Bhatia, D.; McCabe, R. W.; Harold, M. P.; Balakotaiah, V. *J. Catal.* **2009**, *266* (1), 106−119. (e) Getman, R. B.; Schneider, W. F. *ChemCatChem* **2010**, *2* (11), 1450−1460. (f) Wu, C.; Schmidt, D.; Wolverton, C.; Schneider, W. F. *J. Catal.* **2012**, *286*, 88−94.
(28) (a) Kresse, G.; Furthmüller, J. *Comput. Mater. Sci.* **1996**, *6*, 15. (b) Kresse, G.; Joubert, D. *Phys. Rev. B* **1999**, *59*, 1758.
(29) (a) Perdew, J. P.; Chevary, J. A.; Vosko, S. H.; Jackson, K. A.; Pederson, M. R.; Singh, D. J.; Fiolhais, C. *Phys. Rev. B* **2011**, 1−17. (b) Perdew, J. P.; Jackson, K. A.; Pederson, M. R.; Singh, D. J.; Fiolhais, C. *Phys. Rev. B* **1992**, *46* (11), 6671−6687.
(30) Rata, A.; Herklotz, A.; Schultz, L.; Dörr, K. *Eur. Phys. J. B* **2010**, *76* (2), 215−219.
(31) Berger, D.; Fruth, V.; Jitaru, I.; Schoonman, J. *Mater. Lett.* **2004**, *58* (19), 2418−2422.
(32) Royer, S.; Duprez, D.; Kaliaguine, S. *Catal. Today* **2006**, *112* (1−4), 99−102.
(33) Kushima, A.; Yip, S.; Yildiz, B. *Phys. Rev. B* **2010**, *82* (11), 115435.
(34) Mizusaki, J.; Mima, Y.; Yamauchi, S.; Fueki, K.; Tagawa, H. *J. Solid State Chem.* **1989**, *80* (1), 102−111.
(35) (a) Over, H., *ChemInform* **2012**, *43* (33), DOI: 10.1002/chin.201233221; (b) Wang, H.; Schneider, W. F.; Schmidt, D. *J. Phys. Chem. C* **2009**, *113* (34), 15266−15273. (c) Weaver, J. F. *Chem. Rev.* **2013**, *113* (6), 4164−4215.
(36) Niemantsverdriet, A. M. d. J. a. J. W. *Surf. Sci.* **1990**, *233*, 355−365.